BIOCHEMISTRY
including biophysical chemistry & molecular biology
Article

Biochemistry **2011,** *50,* 1799–1807 1799
DOI: 10.1021/bi1016759

A Combined Global and Local Approach to Elucidate Spatial Organization of the Mycobacterial ParB-*parS* Partition Assembly[†]

Barnali N. Chaudhuri,*[‡,§] Sayan Gupta,[||,#] Volker S. Urban,[⊥,#] Mark R. Chance,[||] Rhijuta D'Mello,[||] Lauren Smith,[‡,¶] Kelly Lyons,[‡,○] and Jessica Gee[‡,▽]

[‡]*Hauptman Woodward Institute, and* [§]*Department of Structural Biology, University of Buffalo, 700 Ellicott Street, Buffalo, New York 14203, United States,* [||]*Center for Proteomics and Bioinformatics, Case Western Reserve University, Cleveland, Ohio 44106-4965, United States, and* [⊥]*Center for Structural Molecular Biology, Oak Ridge National Lab, Oak Ridge, Tennessee 37831-6142, United States.* [#]*These authors contributed equally to the project.* [○]*Current address: Lake Erie College of Osteopathic Medicine, 1858 W. Grandview Boulevard, Erie, Pennsylvania 16509-1025.* [▽]*Division of Infectious Diseases, University of Pittsburgh, 3550 Terrace Street, Pittsburgh, Pennsylvania 15261.* [¶]*Current address: Waste Stream Technology, Inc., 302 Grote Street, Buffalo, New York 14207.*

Received October 18, 2010; Revised Manuscript Received December 9, 2010

ABSTRACT: Combining diverse sets of data at global (size, shape) and local (residue) scales is an emerging trend for elucidating the organization and function of the cellular assemblies. We used such a strategy, combining data from X-ray and neutron scattering with H/D-contrast variation and X-ray footprinting with mass spectrometry, to elucidate the spatial organization of the ParB-*parS* assembly from *Mycobacterium tuberculosis*. The ParB-*parS* participates in plasmid and chromosome segregation and condensation in predivisional bacterial cells. ParB polymerizes around the *parS* centromere(s) to form a higher-order assembly that serves to recruit cyto-skeletal ParA ATPases and SMC proteins for chromosome segregation. A hybrid model of the ParB-*parS* was built by combining and correlating computational models with experiment-derived information about size, shape, position of the symmetry axis within the shape, internal topology, DNA−protein interface, exposed surface patches, and prior knowledge. This first view of the ParB-*parS* leads us to propose how ParB spread on the chromosome to form a larger assembly.

Multidrug resistance and an ability to stay in latent state by arresting growth are key problems in combating the deadly, infectious, and slow-growing pathogen *Mycobacterium tuberculosis* (MTB(*1*)). There is renewed interest in understanding those basic cell cycle processes, such as the segregation of chromosomes followed by cell division, in MTB in a search for new therapeutics (*2*, *3*). Although eukaryotic mitotic segregation is well-studied, our understanding of how bacteria segregates newly replicated chromosomes prior to cell division is just beginning to emerge (*4*−*6*). The segrosome or the partition cassette (ParABS) is linked to an array of crucial cellular processes including plasmid/chromosome pairing, segregation and condensation, and replication initiation as well as cytokinesis (*4*−*13*). In *Mycobacterium*, loss or malfunction of segrosome genes leads to a higher frequency of anucleated, nonviable cells and perceptible growth defects (*14*, *15*).

Segrosome is among the growing list of bacterial cytoskeletal elements that play important roles in moving and positioning of the assemblies within the cell in a space and time-dependent manner (*16*). The segrosome is composed of two proteins (ParA and ParB) and a set of centromere-like, origin-proximal DNA sequences (*parS*). ParBs spread by polymerizing on the *parS*-adjacent chromosomal DNA to form the partition complex (*5*, *17*, *18*), a large assembly covering >1 kb that serves to recruit ParA as well as other proteins (such as structural maintenances of chromosome or SMC protein, 12−13) in several bacteria. ParA belongs to the Walker-like cytoskeletal ATPases family that moves chromosomes probably by nucleotide dependent disassembling (*6*, *19*). Little is known about the architecture of the chromosomal ParB−DNA partition complex and how it recruits ParA, leading to chromosome movement.

ParBs are multidomain, flexible, and multimeric, and are largely α-helical in nature (*20*). Chromosomal and plasmid ParBs are diverse in lengths and sequences. ParB utilizes either classical helix-turn-helix (HTH) motifs or ribbon-helix-helix motifs for protein−DNA interactions (*20*). Although progress has been made in structure determination of the ParBs from plasmids, structural data on how chromosomal ParB interacts with the *parS* centromere is sparse due to crystallization challenges (*21*). As an alternative, hybrid approaches provide a way

---

[†] B.N.C. acknowledges Oishei Foundation for funding. SANS research at Oak Ridge National Laboratory's Center for Structural Molecular Biology is supported by the Office of Biological and Environmental Research, using facilities supported by the U.S. Department of Energy, managed by UT-Battelle, LLC under contract No. DE-AC05-00OR22725. Work at the Center for Synchrotron Biosciences and Center for Proteomics, Case Western Reserve University, is supported by the National Institute for Biomedical Imaging and Bioengineering under grants R01-EB-09688 and P30-EB-09998. The National Synchrotron Light Source at Brookhaven National Laboratory is supported by the Department of Energy under Contract DE-AC02-98CH10886. Work at the Stanford Synchrotron Radiation Laboratory was supported by the Department of Energy, Office of Biological and Environmental Research, and by the National Institutes of Health, National Center for Research Resources, Biomedical Technology Program.

*Corresponding author. Hauptman Woodward Institute, 700 Ellicott St., Buffalo, NY 14203. Phone: +1 716 898 8681. Fax: +1 716 898 8660. E-mail: bchaudhuri@hwi.buffalo.edu.

Abbreviations: LC-MS, liquid chromatography−mass spectrometry; MTB, *Mycobacterium tuberculosis*; SAS, small angle scattering; SAXS, small-angle X-ray scattering; SANS, small angle neutron scattering; XF, X-ray footprinting.

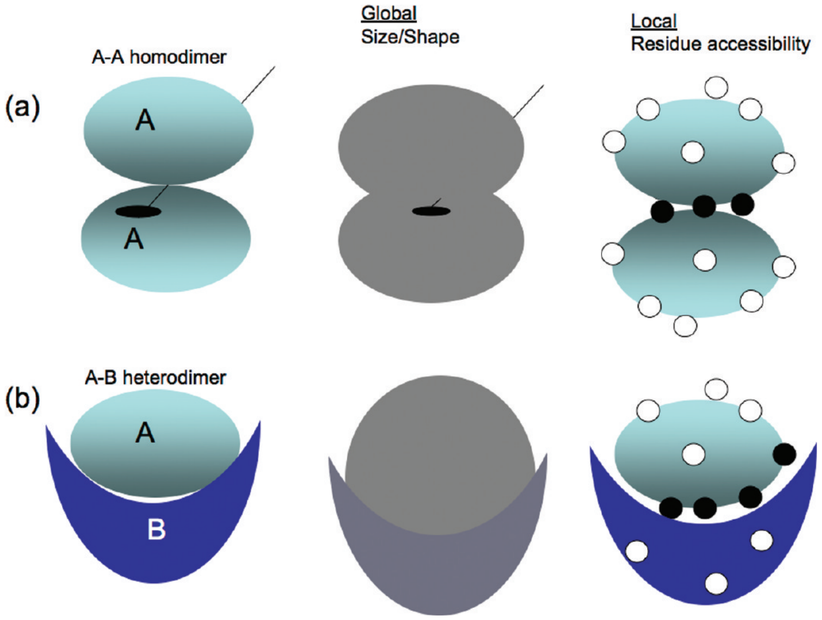

FIGURE 1: Schematic representation depicting complimentarity between the global shape and local residue-accessibility information is shown for two simple assemblies: (a) a symmetric homodimer A−A (the dyad axis is shown as a black line) and (b) a heterodimer A−B (black circles, protected residues; white circles, accessible residues).

to systematically investigate the organization of the assembly formed by ParB at and around the *parS* and its function.

Integrating data obtained from a variety of experimental sources to understand organization and function of cellular assemblies is an emerging trend (*22*, *23*). Recent successful examples include combining protein footprinting with docking (*24*), electron microscopy with comparative modeling (*25*), chemical cross-linking/mass spectrometry (MS) with small angle scattering (SAS) in solution (*26*), SAS with crystallography/NMR/MS, and modeling (*27*−*31*) to elucidate organization of the biological assemblies.

Solution scattering is emerging as a popular method due to the relative ease of obtaining size and low resolution shape information suitable for evaluating competing hypotheses about point-group symmetry and assembly organization (*28*, *29*, *32*, *33*). Combination of multiple X-ray as well as neutron scattering with contrast variation aids in robust shape computation and the determination of internal topology in a two component system (*34*−*37*). Although SAS has modest information content, it is very instructive in judicious combination with additional experimental data.

X-ray footprinting, a novel, powerful technique comparable to traditional DNA footprinting, provides local residue accessibility information on proteins (*38*−*42*). Residues with reduced interactions with solvents upon macromolecular assembly effectively describe the interaction interface. A map of the interaction interface as well as exposed, accessible residues combined with global shape, size, symmetry, topology information, and structural models of the components provides a rather potent way to elucidate assembly architecture (Figure 1).

We have used a hybrid strategy, by correlating data on global (small-angle X-ray and neutron scattering with H/D-contrast variation or SAXS/SANS) and local (X-ray footprinting or XF) scales, coupled to computational modeling and data-driven docking, to elucidate the low resolution solution organization of the ParB-*parS* assembly from MTB. This first view of the spatial organization of mycobacterial ParB-*parS* allows us to propose a model for the spreading of ParB on the *parS*-adjacent chromosome.

EXPERIMENTAL PROCEDURES

Expression and Purification of ParB. Mycobacterial ParB (tbParB, clone gifted by Dr. C.-Y. Kim, LANL) was expressed in BL21(DE3) competent cells in LB media. The cell pellets were resuspended in lysis buffer containing 50 mM Tris·HCl at pH 8, 500 mM NaCl, 10% glycerol, and 5−10 mM imidazole, and lysed using a microfluidizer (Microfluidics Corp.). The cell lysate was loaded onto a Nickel-affinity column (HiTrap Chelating HP, GE Lifesciences) and eluted with an imidazole gradient. After the run, the fractions of interest were dialyzed overnight in the following buffer: 10 mM Tris at pH 8, 150 mM NaCl, and 10% glycerol. The dialyzed volume was centrifuged to remove precipitants, filtered, and run on an ion-exchange column (Capto Q or Mono Q HR 10/10, GE Lifesciences) to remove DNA. The last run was a size-exclusion column (HiLoad 16/60 Superdex 200, GE Lifesciences) using the following buffer A: 10 mM Tris at pH 8, 150 mM NaCl, and 10% glycerol. Typically, two well-separated peaks were eluted: a high-molecular mass tbParB−DNA complex of unknown nature followed by a tbParB peak.

Preparation of the tbParB-parS Complex. DNA oligonucleotides were purchased from Keck facility, Yale University. DNA was resuspended in 10 mM NaOH, 100 mM NaCl, and purified on a Capto-Q using 10 mM NaOH, 1 M NaCl as elution buffer. Purified DNA was dialyzed against water, ethanol precipitated, and resuspended in TN buffer (10 mM Tris, pH 8.0, and 150 mM NaCl). DNA was annealed by heating for 10 min at 95 °C and slow cooling.

Purified tbParB protein (∼37 kDa/monomer) was added slowly to duplex *parS22* DNA (GGATGTTTCACGTGAAACATCC; the 14-meric *parS* sequence is underlined) in 2:1 (protein/DNA) molar ratio. The tbParB-*parS22* complex was concentrated to a final protein concentration of up to ∼5−7 mg/mL in buffer A for subsequent SAS analysis.

Electrophoretic Mobility Shift Assay. Duplex oligonucleotides (*parS22*, 250 nM) with and without tbParB (1 μM) were run in a 4−20% polyacrylamide gel for 1 h (110 V) in Tris-borate-EDTA buffer (MiniProtean, BioRAD). Following the run, the gel was stained in SYBR-green dye and photographed using a gel-imaging system.

Solution X-ray Scattering Experiment. SAXS data was collected at the BL4-2 beamline at Stanford Synchrotron Radiation Laboratory, Stanford, using a standard beamline setup: 1.7 m detector distance and 1−5 s exposures. Data sets for tbParB-*parS22* were collected at 3 concentrations (Supporting Information, Figure S1a). Initial data analysis did not reveal any significant aggregation, interparticle interference, or radiation damage effect. Data analysis was performed using the ATSAS suite (*43*). R_gs were obtained from Guinier analysis of the low angle data ($q \cdot R_g \leq 1.3$, computed using PRIMUS from the ATSAS suite). R_gs values were averaged over 3 concentrations and showed no concentration dependence (within 5% of the average) at the experimental conditions. Multiple test runs were performed using GNOM for estimating $D_{\max}$ from the pair distribution function (Supporting Information, Figure S1b). CREDO (*43*) was used for missing domain reconstruction.

Solution Neutron Scattering with Hydrogen/Deuterium (H/D) Contrast Variation. SANS experiments were performed at the CG-3 Bio-SANS instrument (*44*) at the High Flux Isotope Reactor facility of Oak Ridge National Laboratory, using a neutron beam with 6 Å wavelength, wavelength spread $\lambda/\Delta\lambda = 0.15$, and 2.5 m sample to detector distance, which covered an effective range of momentum transfer $0.013\ \text{Å}^{-1} \leq q \leq 0.39\ \text{Å}^{-1}$. $q = (4\pi/\lambda)\sin\theta$ and 2θ is the scattering angle. The samples were series-dialyzed in buffer (10 mM Tris·HCl at pH 8.0 and 10% glycerol) containing varying amounts of D_2O before exposure. Sample scattering (tbParB-*parS22*, at 3 mg/mL concentration) was measured using circular, quartz cells with 1 mm path length and 300 μL volume at 15 °C temperature and 1−4 h exposure time. The scattering intensity profiles $I(q)$ versus q were obtained by azimuthally averaging the processed 2D images, which were normalized to incident beam monitor counts and corrected for detector dark current, pixel sensitivity, and solvent scattering backgrounds from the buffer and quartz cell. Experimental scattering intensity was converted to absolute neutron scattering cross-section per unit volume, $d\Sigma/d\Omega$ in units of cm^{-1} by calibration with a scattering standard of known cross-section (*45*). The average molecular mass of the complex, M_w, was estimated from the absolute cross-section extrapolated to $q = 0$ using the relationship

$$\lim_{q \to 0} (d\Sigma/d\Omega) = c \cdot M_w \cdot (\rho - \rho_0)^2 / N_A \cdot d_m^2$$

which holds for noninteracting scattering particles (*46*). Here, c is the concentration of the scattering object (mass/volume), d_m is its average mass density, and N_A is Avogadro's constant. ρ and ρ_0 are the average scattering length density of the complex and the scattering length density of the buffer, respectively. Percent of D_2O for each sample was recalculated using neutron transmission data. Buffer subtraction, correction for in-coherent scattering (using high-angle data), and subsequent data processing were performed using Igor-Pro (http://www.wavemetrics.com/) based software developed at ORNL. Contrast values were calculated using MULCH (*47*). MONSA and other ATSAS suite of programs (*43*) were used for data analysis and shape reconstructions. The DAMAVER package (*43*) was used for averaging shapes obtained from multiple independent calculations. One of the MONSA bead models was used as a reference for aligning final averaged protein and DNA shapes using SUPCOMB (*43*).

Synchrotron X-ray Radiolysis. tbParB and tbParB-*parS22* complexes (2−4 μM, with slightly excess DNA) in 10 mM phosphate, pH 7.0−7.5, and 150 mM NaCl were exposed to synchrotron X-ray white light at the National Synchrotron Light Source's (Brookhaven National Laboratory) beamline X-28C (*41*). The X-ray beam parameters were optimized by using the Alexa fluorophore assay. Samples were irradiated (0−40 ms) using a modified KinTek (KinTek Corporation) apparatus at room temperature. The samples were collected in methionine-amide (10 mM) to rapidly quench any secondary oxidation. Samples were frozen in dry ice and stored at −80 °C.

Liquid Chromatography−Mass Spectrometry (LC-MS) and Data Analysis. Samples were digested with trypsin (sequencing grade modified trypsin, Promega) and analyzed by LC-ESI/MS and MS/MS using a Water 2695 LC systems (Dionex) with a reversed-phase C18 column (Vydac Inc.), interfaced to a LCQ-Deca XP mass spectrometer (Thermo-Finnigan). MS/MS spectra of the peptide mixtures (Supporting Information) were searched against the tbParB sequence for modifications (*38−40*) of the peptides. Levels of modification versus exposure time were plotted and fitted with a single exponential function with Origin version 7.5 (OriginLabs) to determine the rate-constants of peptide modification. The Origin program, using 95% confidence limits of the fitting results, determined the reported errors of the rate-constant data. Samples exposed to X-rays in repeated experiments (in triplicate) exhibited consistently similar extent of labeling on the same residues.

Computational Modeling and Docking. I-TASSER (*48*) and MAKE-NA (http://structure.usc.edu/make-na) were used for computing structural models. A perl script was written for extracting the direction cosines of the dyad axes within the dimeric N-terminal domains of the tbParB and the palindromic DNA. Graphics package O (*49*) was used for all manual manipulations of the models and docking. The dyad axes of the protein and the DNA models were manually aligned with the dyad axis of the shape map (the *z*-axis) in graphics while docking, followed by rotation about this axis to obtain a visual best-fit to the shape map. Figures were prepared using MOLSCRIPT (*50*).

RESULTS

Computational Models of Components of the ParB-parS assembly. Models of the individual domains of tbParB and *parS* DNA were built computationally. The tbParB can be divided into two domains: the N-terminal domain (tbParB-N) spanning the first 260 residues and the C-terminal domain (tbParB-C) containing the last 84 residues. We used the crystal structure of the N-terminal domain of ParB from *Thermus thermophilus* (PDB code 1vz0, thmParB-N (*21*)), with which tbParB shares 42% sequence identity, for building a homology model of the tbParB-N (residues 60−258; C-score −1.3 (*48*)). As the pdb model 1vz0 does not contain the segment corresponding to the first 59 residues of the tbParB, we were not able to model this part. This N-terminal extended region and the first 23 residues of the C-terminal domain of tbParB were predicted to be disordered (GLOBPLOT (*51*)). Inclusions of these predicted disordered regions produced models with poor scores and therefore were not included in structural modeling. The tbParB-C does not have significant sequence similarity to any structure in the PDB. Therefore, an *ab initio* model of the truncated tbParB-C was built (residues 284−344, C-score −1.08, and TM-score 0.57 (*48*)). A 22-meric, palindromic, duplex DNA containing the *parS* site,

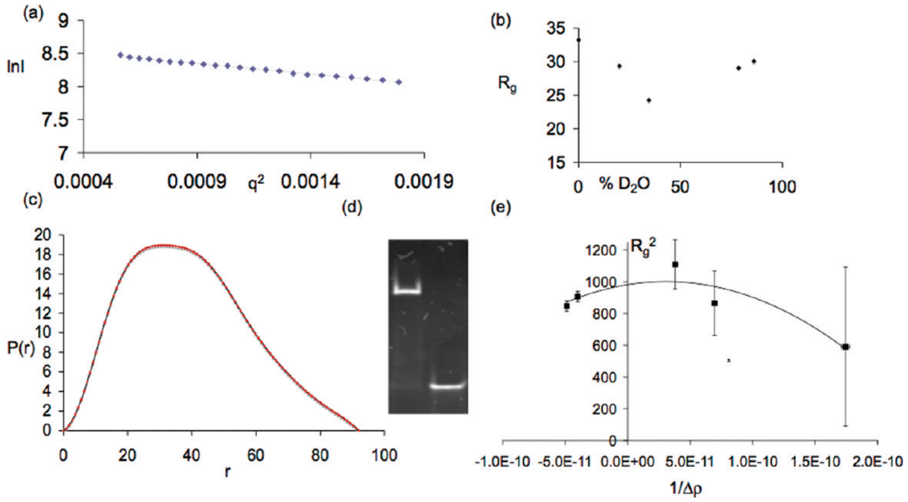

FIGURE 2: Molecular size of the tbParB-*parS22* assembly. (a) Guinier plot (ln I versus q^2, $\ln[I(q)] = \ln[I(0)] - (q^2R_g^2)/3$; I is the intensity; $I(0)$ is the intensity at 0 scattering angle; R_g is in Å; q is the moment transfer in $Å^{-1}$) is shown for the low-angle region of the X-ray scattering profile of the tbParB-*parS22*. R_g was determined to be 31.5 Å, averaged over 3 concentrations. (b) Plot of the Guinier R_g versus % D_2O (0%, 20%, 34.5%, 78.5%, and 86%) is shown for the 5 SANS data sets. (c) Plot of the pair distribution function $P(r)$ versus pairwise distance r in Å for the tbParB-*parS22* complex ($r_{min} = 0$; $r_{max} = 92$ Å; real space $R_g = 30.4$ Å; calculated using GNOM using the SAXS data (*43*)). (d) Electrophoretic mobility shift assay shows tbParB-*parS22* assembly formation (left lane, tbParB-*parS22*; right lane, *parS22*). (e) Stuhrmann plot (R_g^2 in $Å^2$ versus inverse contrast ($1/\Delta\rho$); contrast in cm^{-2} (*51*)) obtained from the 5 SANS data sets. The continuous black line represents a second-degree polynomial fit to the data ($R_g^2 = -20549(1/\Delta\rho^2) + 1258(1/\Delta\rho) + 981.5$). The data set with 34.5% D_2O near the protein match-point was very weak and was not included in the shape computation.

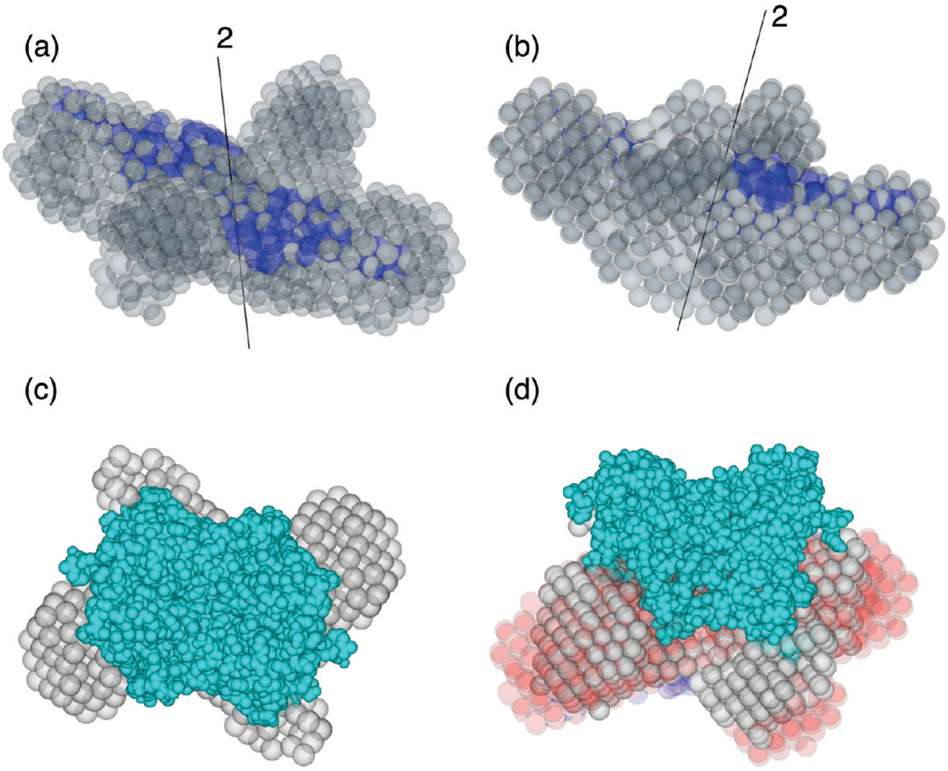

FIGURE 3: Molecular shape and internal topology of the tbParB-*parS22* assembly. (a,b) Different views of the averaged, *ab initio* reconstructed shape of the tbParB-*parS22* complex (all of the shapes here and elsewhere are shown as beads in CPK with bead radius = 2.8 Å). The 2-fold symmetry axis is shown as a black line. The averaged DNA phase is shown in blue, and the averaged protein phase is shown in gray. (c,d) Two views of the averaged missing region reconstructed (shown as gray, semitransparent CPK; $\langle\chi\rangle = 2.6$, NSD = 1.5 for 5 cases) using the SAXS data of the tbParb-*parS22* assembly and the coordinates of the partial atomic model of the tbParB-N. The model of the tbParB-N dimer is shown as cyan CPK. The corresponding *ab initio* model is shown as semitransparent red (protein) and blue (DNA) beads in 3D.

henceforth referred to as *parS22*, was built in the B-form with standard geometry. In the absence of a crystal structure of the entire chromosomal ParB or its complex with DNA, these computational models of the tbParB-N, the *parS22*, and the tbParB-C were subsequently combined to interpret the solution scattering and the protein footprinting data.

Size and Mass of the ParB-parS Assembly from Solution Scattering. Analyses of the solution scattering data sets obtained from the tbParB-*parS22* provided information on size parameters such as the radius of gyration (R_g) and maximum particle diameter (D_{max}) of the assembly (Figure 2a−c). Assembly formation between tbParB and *parS22* was shown *in vitro* by the electrophoretic mobility shift assay (Figure 2d). Both SAXS and SANS data (at 0% D_2O) of the tbParB-*parS22* yielded a D_{max} of 92 Å. These model-free parameters served as useful restraints for molecular shape calculations.

The molecular mass of the tbParB-*pars22* complex was estimated to be 84 kDa ± 10% from the absolute scattering cross-section of the SANS data for lim $q \to 0$. This value is in excellent agreement with the expected mass of the tbParB-*parS22* assembly with a 2:1 stoichiometry. This cross-check is important because it confirms that the SANS data stems from individual tbParB-*parS22* complexes and that interparticle interaction or larger sized aggregates do not significantly interfere with data interpretation. The Stuhrmann plot obtained a negative value of alpha (Figure 2e (*52*)), indicating a lower scattering density for the peripheral component in a two-component model. R_g at the infinite contrast was determined to be 31.3 Å from the Stuhrmann plot.

Molecular Shape of the ParB-parS Assembly. Shape of the tbParB-*parS22* assembly was computed *ab initio* by combining multiple scattering curves (Supporting Information). As DNA scatters differently than proteins, a two-phase modeling approach was used (*35*). Four SANS profiles for the tbParB-*parS22* assembly in varying ratios of H_2O/D_2O were combined with two SAXS profiles (one for the entire tbParB-*parS22* complex and one containing theoretical SAXS data for the *parS22* DNA) for shape computation. Multiple parallel shape reconstructions were performed while imposing a 2-fold symmetry constraint in each case. Five such resultant shapes (set of points in Cartesian space or beads) were superposed, followed by the calculation of a mean normalized spatial discrepancy measure or NSD ($NSD_{protein} = 0.9$; $NSD_{DNA} = 0.6$ (*53*)). Discrepancies or the square-root of the chi-values (χ) between model and data were < 2 for all six curves ($\langle\chi\rangle = 1.4$ for 5 cases; the fits of the model and data are shown in Supporting Information, Figure S1c−h). Releasing the 2-fold symmetry did not alter the discrepancy between model and data ($\langle\chi\rangle = 1.4$, $NSD_{protein} = 0.85$, and $NSD_{DNA} = 0.8$ for 5 cases), further supporting the expected C_2 point-group symmetry of the tbParB-*parS22* assembly. This averaged shape was used for subsequent docking (Figure 3a,b).

Although one-dimensional solution scattering profiles do not provide a unique molecular shape, persistent features observed in multiple independently computed shapes should reveal the average, solution-phase shape of the molecule at low-resolution. A comparison of the bead models of the tbParB-*parS22* revealed its spatial assembly (Figure 3a,b and Figure Si-l, Supporting Information). Although disordered regions were predicted within the tbParB sequence, the resultant shape of the DNA-bound tbParB was rather compact. The shape and orientation of the

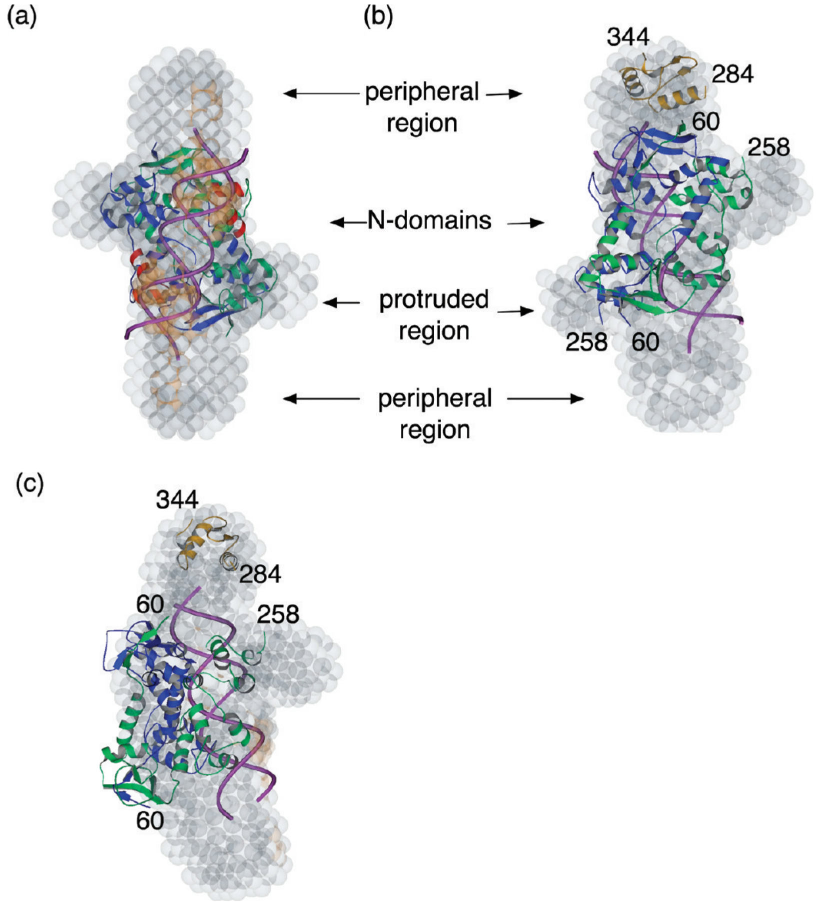

FIGURE 4: Docking of the tbParB-*parS22* assembly components in the SAS shape. (a−c) Different views of the docked components of the tbParB-*parS22* are shown with the averaged shape (semitransparent CPK; protein beads are gray; DNA beads are orange). Two subunits of the truncated, comparative model of the tbParB-N are shown as blue and green cartoons. DNA is shown in violet. The HTH motifs within the tbParB-N are shown in red in panel a. An *ab initio* model of the truncated tbParB-C is shown in yellow (b,c). The N- and the C-terminal ends of the protein fragments are marked in panels b and c. Distance between the Cα atoms of the 284th residue and the nearest 258th residue is 23 Å in this model. Only one of the two 2-fold related tbParB-C domains is shown in the figure.

Table 1: Hydroxyl Radical Modification Rate Constants

			rate constant k (sec^{-1})[d]		
sequence number[a]	sequence of the tryptic fragment[b]	modification Sites[c]	tbParB	tbParB-*parS22*	ratio of $k_{\text{ParB-parS}}/k_{\text{ParB}}$
14−36	GLAALIPTGPADGESGPPTLGPR	14−36	1.4 ± 0.1	1.2 ± 0.1	0.9
37−61	**M**GSATADVVIGGPVPDTSV**M**GAIYR	M37, M56[e]	103.1 ± 8.5	137.0 ± 11.2	1.3
62−73	EIPPSAI**E**ANPR	E69	0.7 ± 0.1	0.6 ± 0.1	0.9
77−92	QV**FDEE**ALAE**LVH**SIR	peak 1 F79, D80, E81, E82	peak 1 2.3 ± 0.3	peak 1 2.0 ± 0.5	peak 1 0.9
		peak 2 L87, V88, H89	peak 2 1.0 ± 0.3	peak 2 1.1 ± 0.3	peak 2 1.1
93−103	E**F**GLLQPIVVR	F94	0.30 ± 0.02	0.70 ± 0.06	2.3
104−113	SLAGSQTGVR	−	−	−	−
114−121	YQIV**M**GER	M118	15.3 ± 1.0	11.0 ± 1.2	0.7
125−139	AAQEAGLATIPAIVR	−	−	−	−
140−148	ETGDDNLLR	−	−	−	−
149−157	DALLENI**H**R	H156	0.30 ± 0.02	0.15 ± 0.01	0.5
158−186	VQLNPLEEAAAYQQLLDEFG**VTH**DELAAR	178−180	1.5 ± 0.2	0.8 ± 0.2	0.5
190−199	SRPLITN**M**IR	M197	7.9 ± 0.7	4.9 ± 0.6	0.6
203−209	LPIPVQR	−[g]	−	−	−
211−222	VAAGVLSAG**H**AR	H220	0.60 ± 0.02	0.12 ± 0.02	0.2
223−240	ALLSLEAGP**E**AQ**EE**LASR	E232,E235, E236	0.50 ± 0.04	0.52 ± 0.05	1.0
241−249	IVAEGLSVR	−	−	−	−
250−264	ATE**ETVTLAN**HEANR	253−259	0.80 ± 0.07	0.40 ± 0.06	0.5
265−278	QA**H**HSDATTPAPPR	H267[f]	−	−	−
279−293	RKPIQ**MP**GLQDVAER	M284, P285	31.5 ± 3.0	25.0 ± 2.8	0.8
294−301	LSTTFDTR	−	−	−	−
302−308	VTVSLGK	−	−	−	−
313−325	IVVEFGSVDDLAR	313−325	< 0.1	< 1.0	not reported
326−335	IVGL**M**TTDGR	M330	0.9 ± 0.1	0.9 ± 0.1	1.0

[a] > 90% sequence coverage was obtained from the LC-MS analysis of trypsin fragments. [b] Sequences of tryptic fragments and position of modified residues, which were identified by ESI-MS and confirmed by MS/MS analysis. Modifies peptide fragments were eluted as a single peak or multiple peaks. [c] Modified residue identified by MS/MS. Mass shift of +14 Da (carbonylation), +16 Da (hydroxylation), and +32 Da (double oxidation at Met) were detected as major modification products. A single modification peak contained one (e.g., E69 for the fragment 62−73) or several (mixed) modification products (e.g., 158−186). [d] Rate constants were estimated by employing a single exponential fit of hydroxyl radical modification data to a first order decay as described in Experimental Procedures. [e] +16 Da modification products of M37 and M56 eluted as separate peaks, but their double oxidation product +32 Da eluted as a single peak. [f] +16 Da modification peak of H267 was detected. The rate constant cannot be evaluated because of inconsistency in the abundance of the modified species in the mass spectrometer. [g] "−" indicates no modification was detected.

centrally located, dyad-symmetric DNA phase (high scattering beads in a two-bead model, 14% of the total volume) was clear. Thus, SANS contrast variation data made the shape computation process robust and aided in elucidating internal topology.

We used a partial atomic model of the tbParB-N and SAXS data for the entire tbParB-*parS*22 assembly to reconstruct the missing region as uniformly scattering beads (*54*), while imposing 2-fold symmetry. Resultant shapes of the multiply reconstructed missing region closely resembled those obtained from the *ab inito* reconstructions (superposed using SUPCOMB (*43*), NSD 0.9, Figure 3c,d), lending further support to our model. Rigid-body modeling was not attempted due to the incompleteness of our input models.

Structural Interpretation of the ParB-parS Shape. Although solution scattering shapes do not represent high-resolution molecular envelopes, they provide valuable insights about low-resolution spatial organization of the molecules and molecular assemblies. Averaged shape obtained from SAXS/SANS was combined with the computational models to elucidate organization of the tbParB-*parS* partition complex (Figure 4). The model of the *parS22* DNA was docked into the DNA phase of the averaged shape by aligning their dyad axes and rotating around this axis for visual best fit. Similarly, the model of the truncated, dimeric tbParB-N, modeled after thmParB-N (*20*), was docked into the protein phase of the shape. The HTH motifs within the thmParB-N dimer are separated by ∼34 Å, poised for docking into the major groove of DNA (*21*). The HTH motifs of the tbParB-N dimer were docked into the major groove of the *parS22* moiety.

Additional space occupied by the protein beads within the overall shape was adequate for accommodating other missing protein regions. The protruded region within the shape (Figure 4) is not large enough to accommodate the entire 84-residue C-terminal domain. However, the peripheral space could realistically accommodate the truncated tbParB-C (residues 284−344) as well as the N-terminal extension (residues 1−59). The truncated model of the C-terminal polymerization domain was allocated to the peripheral region of the shape, which is compatible with its biological role. The partial atomic model of the tbParB-C was fitted comfortably within this peripheral space in several physically plausible orientations (Figure 4), leaving room for the rest of the protein chain. Allocation of the C-terminal region in the peripheral space was further supported by a compact solution shape of the tbParB-N in apo form (data not shown).

Local Residue Accessibility Data Supports the ParB-parS Model. X-ray induced hydroxyl-radical footprinting combined with mass spectrometry provided local information on the hydroxyl radical-accessible residues in the tbParB and the tbParB-*parS22* complex (Table 1 and Supporting Information), from which putative interface residues were inferred. Mass spectrometric analyses of the proteolytic digests of the radiolyzed samples were performed for identifying the exact locations of the modified (i.e., accessible) residues. The extents of modifications

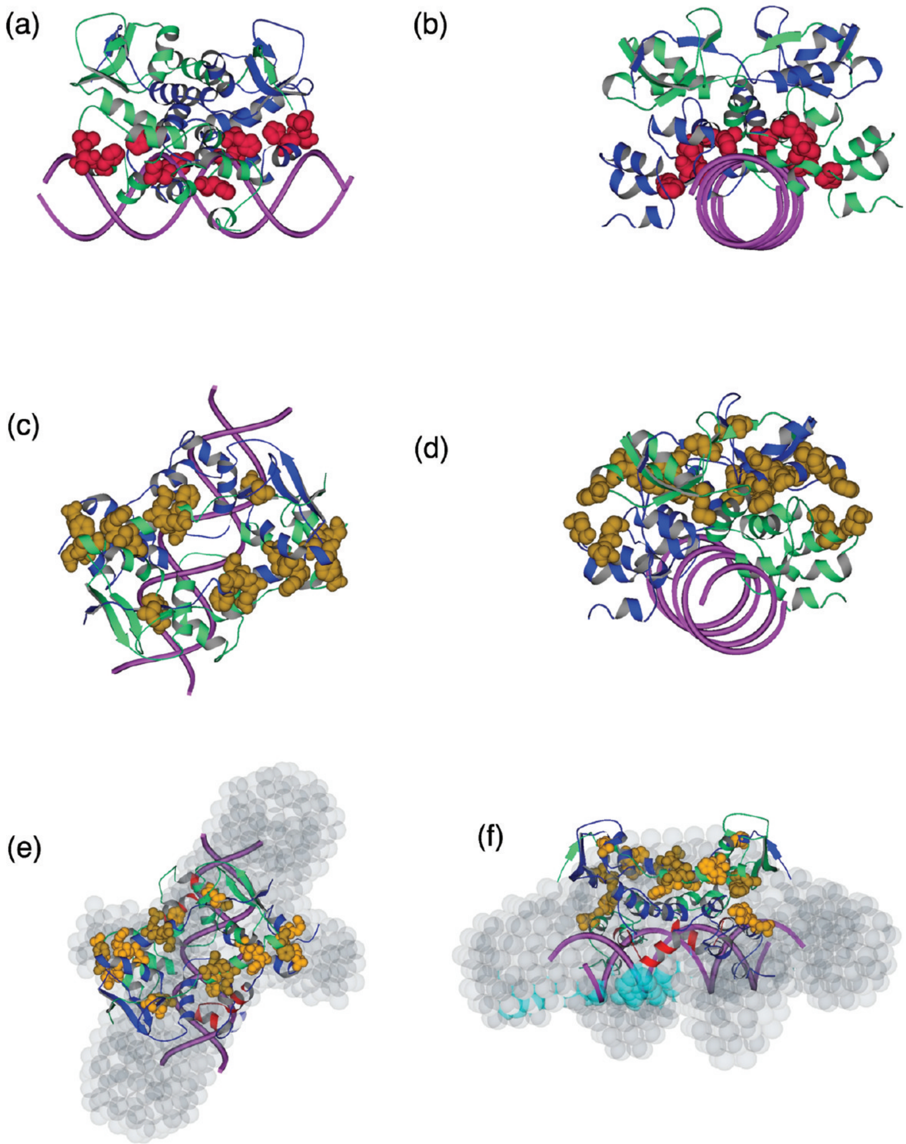

FIGURE 5: X-ray footprinting of the tbParB-*parS22*. (a,b) Two views of the tbParB-N-*parS22* DNA−protein interface (residues 156, 178−180, 197, 220; Table 1). Protected residues are shown as red CPK. Two subunits of the tbParB-N are shown in green and blue. DNA is shown in violet. (c,d) Exposed surface patches (residues 69, 79−82, 87−89, 94, 118, 232, and 235−236; golden-yellow CPK; Table 1) are mapped on the tbParB-N-*parS22*. (e,f) Exposed surface residues, mapped into the tbParB-*parS22* assemblies within the SAS-derived average shape, are shown in golden-yellow CPK. Two HTH motifs (residues 178−204) within the tbParB-N dimer are shown in red. DNA beads are shown in cyan, and the protein beads are shown in gray.

were plotted against irradiation times, and the rate-constants of modifications (*k*) were determined from the X-ray dose−response plots (Supporting Information, Figure S4). The modification rates for the residues (Table 1) provided a quantitative measure of solvent accessibility with high structural resolution (*38*−*40*). The tbParB-*parS* interaction interface was identified by comparing the rate constants between the DNA-free and the DNA-bound states ($k_{\mathrm{ParB}}/k_{\mathrm{ParB}\text{-}parS} < 0.7$ for a protected residue; Table 1). Analysis of the rate constant ratios indicated that the tbParB-N directly interacts with the *parS22* DNA (Figure 5a,b and Table 1). Several protein residues near the *parS22* DNA in our docked model, such as those surrounding the HTH motif (residues 178−204) and the C-terminal end of the tbParB-N (residues 253−259), showed increased protection in the DNA-bound form.

Footprint of all those residues that did not change their accessibility state upon DNA-binding on the tbParB-N ($k_{\mathrm{ParB}}/k_{\mathrm{ParB}\text{-}parS} \sim 1$, Table 1; Figure 5c,d) are indicative of exposed surface patches. These accessible patches are expected to be not covered by either the *parS22* DNA or other regions of the tbParB, such as the C-terminal domain. All these exposed residues in the docked model of the tbParB-N-*parS22* were on or near the surface of the shape (Figure 5e,f), thus supporting out model.

Plausible Models of Spreading of the ParB on the parS-Proximal Chromosome. Disposition of the protein beads with respect to the long axis of the DNA beads in the solution scattering bead model of the tbParB-*parS22* assembly provided a visual clue about how tbParB might spread on an undistorted DNA. We built a testable model of the tbParB-DNA assembly by positioning this bead model in and around a long DNA molecule under the condition that the HTH motifs of the adjacent assemblies interact locally with the major groove of the DNA (Figure 6a,b). The adjacent C-terminal polymerization domains

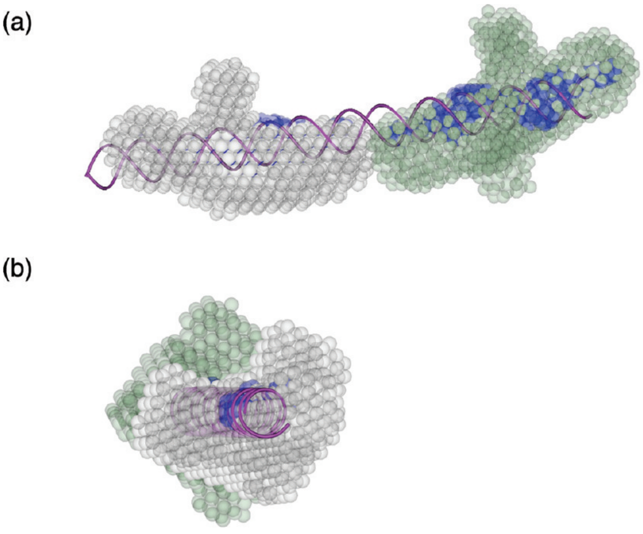

FIGURE 6: Proposed model of the higher-order partition complex. (a, b) Polymerization of tbParB (bead model, semitransparent CPK) is shown on a long DNA (in violet). Protein beads of the adjacent dimeric tbParB-*parS22* units are colored in gray and light-green. DNA beads are colored in blue.

are positioned near DNA in this model. Although the tbParB-C does not appear to make any contact with the short *parS22* DNA (Table 1), it contains several positively charged residues (theoretical pI 9.8). Some of these basic residues are expected to shield the DNA phosphate groups while spreading on the chromosome, as shown in our model (Figure 6a,b). In comparison, theoretical pI of the N-terminal extension of the tbParB (residues 1−59) is 3.3, which rules out its interaction with the DNA. Probably, a longer piece of DNA will be required to demonstrate any possible direct tbParB-C-DNA interaction, allowing evaluation of this proposed mode of spreading.

DISCUSSION

We used solution X-ray and neutron scattering to characterize low resolution shape, size, symmetry, and stoichiometry of the tbParB-*parS22* assembly. Position of the DNA moiety within the assembly was nicely elucidated by the neutron scattering H/D contrast variation. In addition, protein footprinting showed that the N-terminal domain of tbParB uses residues encompassing the HTH motifs to interact with the *parS22* DNA. These experimental data were combined with computational models to elucidate assembly organization of the ParB-*parS*.

Delineating the organization of the ParB-*parS* assembly was a fascinating application of a hybrid approach that harnesses the emerging power of structural mass spectrometry combined with solution scattering techniques. SAS is the only available technique that provides spatial information on proteins that are not amenable to crystallization and are too large for NMR but too small for electron microscopy experiments, as is the case with ParB-*parS* complex. Combination of multiple scattering curves with different contrasts, together with the symmetry constraint, aided in robust *ab initio* shape computation and clear identification of the regions occupied by the protein and the DNA phases. Nevertheless, SAS-based shape computation could be ambiguous (such as enantiomer selection) and therefore should be considered with additional data. X-ray footprinting provided crucial, residue-specific information on the protein−DNA interaction interface as well as exposed surface patches. In addition to experimental data, an expectation based on known interactions between HTH motifs of the ParB and the major groove of the DNA was essential in docking. Partial computational models used in this study served the purpose of assigning regions within the overall shape in the absence of an available crystal structure and matched well with all the experimental data. These complementary information elegantly led to the first view of the low-resolution chromosomal ParB-*parS* organization in solution, about which nothing was known.

Bead model of the ParB-*parS* assembly was used as the Lego or building blocks for modeling how ParB might polymerize on the *parS*-proximal DNA to form the higher-order partition complex. It will be possible to test and refine this proposed mode of spreading using a hybrid strategy similar to that described in this article. In addition, our models provide a structural framework for designing experiments to explore how the partition complex participates in the recruitment of ParA or SMC proteins, leading to chromosome segregation and condensation.

ACKNOWLEDGMENT

B.N.C. acknowledges Dr. Tsuruta for advice and assistance with the SAXS experiment, T. Grant for useful discussions, Dr. J. Griffin for critically reading the manuscript, and Dr. C.-Y. Kim from LANL for the tbParB clone.

SUPPORTING INFORMATION AVAILABLE

Four figures (S1−4) describing solution scattering and footprinting data, as described in the text. This material is available free of charge via the Internet at http://pubs.acs.org.

REFERENCES

1. Hett, E. C., and Rubin, E. J. (2008) Bacterial growth and cell division: a mycobacterial perspective. *Microbiol. Mol. Biol. Rev. 72*, 126–156.
2. Nisa, S., Blokpoel, M. C., Robertson, B. D., Tyndall, J. D., Lun, S., Bishai, W. R., and O'Toole, R. (2010) Targeting the chromosome partitioning protein ParA in tuberculosis drug discovery. *J. Antimicrob. Chemother. 65*, 2347–2358.
3. Vollmer, W. (2006) The prokaryotic cytoskeleton: a putative target for inhibitors and antibiotics? *Appl. Microbiol. Biotechnol. 73* (1), 37–47.
4. Hayes, F, and Barillà, D. (2006) The bacterial segrosome: a dynamic nucleoprotein machine for DNA trafficking and segregation. *Nat. Rev. Microbiol. 4*, 133–143.
5. Gerdes, K., Howard, M., and Szardenings, F. (2010) Pushing and pulling in prokaryotic DNA segregation. *Cell 141* (6), 927–942.
6. Ptacin, J. L., Lee, S. F., Garner, E. C., Toro, E., Eckart, M., Comolli, L. R., Moerner, W. E., and Shapiro, L. (2010) A spindle-like apparatus guides bacterial chromosome segregation. *Nat. Cell Biol. 12* (8), 791–798.
7. Ringgaard, S., Löwe, J., and Gerdes, K. (2007) Centromere pairing by a plasmid-encoded type I ParB protein. *J. Biol. Chem. 282* (38), 28216–28225.
8. Mohl, D. A., Easter, J., and Gober, J. W. (2001) The chromosome partitioning protein, ParB, is required for cytokinesis in Caulobacter crescentus. *Mol. Microbiol. 42* (3), 741–755.
9. Thanbichler, M., and Shapiro, L. (2006) MipZ, a spatial regulator coordinating chromosome segregation with cell division in Caulobacter. *Cell 126*, 147–162.
10. Bowman, G. R., Comolli, L. R., Zhu, J., Eckart, M., Koenig, M., Downing, K. H., Moerner, W. E., Earnest, T., and Shapiro, L. (2008) A polymeric protein anchors the chromosomal origin/ParB complex at a bacterial cell pole. *Cell 134*, 945–955.
11. Murray, H., and Errington, J. (2008) Dynamic control of the DNA replication initiation protein DnaA by Soj/ParA. *Cell 135*, 74–84.
12. Sullivan, N. L., Marquis, K. A., and Rudner, D. Z. (2009) Recruitment of SMC by ParB-parS organizes the origin region and promotes efficient chromosome segregation. *Cell 137*, 697–707.
13. Gruber, S., and Errington, J. (2009) Recruitment of condensin to replication origin regions by ParB/SpoOJ promotes chromosome segregation in *B. subtilis*. *Cell 137*, 685–696.

14. Jakimowicz, D.; et al. (2007) Characterization of the mycobacterial chromosome segregation protein ParB and identification of its target in *Mycobacterium smegmatis*. *Microbiology 153*, 4050–4060.
15. Maloney, E., Madiraju, M., and Rajagopalan, M. (2009) Overproduction and localization of *Mycobacterium tuberculosis* ParA and ParB proteins. *Tuberculosis 89*, S65–S69.
16. Thanbichler, M., and Shapiro, L. (2008) Getting organized--how bacterial cells move proteins and DNA. *Nat. Rev. Microbiol. 6* (1), 28–40.
17. Murray, H., Ferreira, H., and Errington, J. (2006) The bacterial chromosome segregation protein Spo0J spreads along DNA from parS nucleation sites. *Mol. Microbiol. 61*, 1352–1361.
18. Breier, A. M., and Grossman, A. D. (2007) Whole-genome analysis of the chromosome partitioning and sporulation protein Spo0J (ParB) reveals spreading and origin-distal sites on the *Bacillus subtilis* chromosome. *Mol. Microbiol. 64*, 703–718.
19. Michie, K. A., and Löwe, J. (2006) Dynamic filaments of the bacterial cytoskeleton. *Annu. Rev. Biochem. 75*, 467–492.
20. Schumacher, M. A. (2008) Structural biology of plasmid partition: uncovering the molecular mechanisms of DNA segregation. *Biochem. J. 412*, 1–18.
21. Leonard, T. A., Butler, P. J., and Löwe, J. (2004) Structural analysis of the chromosome seg.regation protein Spo0J from *Thermus thermophilus*. *Mol. Microbiol. 53*, 419–432.
22. Alber, F., Förster, F., Korkin, D., Topf, M., and Sali, A. (2008) Integrating diverse data for structure determination of macromolecular assemblies. *Annu. Rev. Biochem. 77*, 443–477.
23. Cowieson, N. P., Kobe, B., and Martin, J. L. (2008) United we stand: combining structural methods. *Curr Opin Struct Biol 18*, 617–622.
24. Kamal, J. K., and Chance, M. R. (2008) Modeling of protein binary complexes using structural mass spectrometry data. *Protein Sci. 17*, 79–94.
25. Topf, M., Baker, M. L., Marti-Renom, M. A., Chiu, W., and Sali, A. (2006) Refinement of protein structures by iterative comparative modeling and CryoEM density fitting. *J. Mol. Biol. 357*, 1655–1668.
26. Cowieson, N. P., King, G., Cookson, D., Ross, I., Huber, T., Hume, D. A., Kobe, B., and Martin, J. L. (2008) Cortactin adopts a globular conformation and bundles actin into sheets. *J. Biol. Chem. 283*, 16187–16193.
27. Grishaev, A., Wu, J., Trewhella, J., and Bax, A. (2005) Refinement of multidomain protein structures by combination of solution small-angle X-ray scattering and NMR data. *J. Am. Chem. Soc. 127* (47), 16621–16628.
28. Putnam, C. D., Hammel, M., Hura, G. L., and Tainer, J. A. (2007) X-ray solution scattering (SAXS) combined with crystallography and computation: defining accurate macromolecular structures, conformations and assemblies in solution. *Q. Rev. Biophys. 40*, 191–285.
29. Förster, F., Webb, B., Krukenberg, K. A., Tsuruta, H., Agard, D. A., and Sali, A. (2008) Integration of small-angle X-ray scattering data into structural modeling of proteins and their assemblies. *J. Mol. Biol. 382*, 1089–1106.
30. Tidow, H., Melero, R., Mylonas, E., Freund, S. M., Grossmann, J. G., Carazo, J. M., Svergun, D. I., Valle, M., and Fersht, A. R. (2007) Quaternary structures of tumor suppressor p53 and a specific p53 DNA complex. *Proc. Natl. Acad. Sci. U.S.A. 104* (30), 12324–12329.
31. Pires, R., Hartlieb, B., Signor, L., Schoehn, G., Lata, S., Roessle, M., Moriscot, C., Popov, S., Hinz, A., Jamin, M., Boyer, V., Sadoul, R., Forest, E., Svergun, D. I., Göttlinger, H. G., and Weissenhorn, W. (2009) A crescent-shaped ALIX dimer targets ESCRT-III CHMP4 filaments. *Structure 17* (6), 843–856.
32. Svergun, D. I. (1999) Restoring low resolution structure of biological macromolecules from solution scattering using simulated annealing. *Biophys. J. 76*, 2879–2886.
33. Whitten, A. E., and Trewhella, J. (2009) Small-angle scattering and neutron contrast variation for studying bio-molecular complexes. *Methods Mol. Biol. 544*, 307–323.
34. Petoukhov, M. V., Monie, T. P., Allain, F. H., Matthews, S., Curry, S., and Svergun, D. I. (2006) Conformation of polypyrimidine tract binding protein in solution. *Structure 14* (6), 1021–1027.
35. Petoukhov, M. V., and Svergun, D. I. (2006) Joint use of small-angle X-ray and neutron scattering to study biological macromolecules in solution. *Eur. Biophys. J. 35* (7), 567–576.
36. Perkins, S. J., Okemefuna, A. I., Fernando, A. N., Bonner, A., Gilbert, H. E., and Furtado, P. B. (2008) X-ray and neutron scattering data and their constrained molecular modeling. *Methods Cell Biol. 84*, 375–423.
37. Grossmann, J. G., Callaghan, A. J., Marcaida, M. J., Luisi, B. F., Alcock, F. H., Tokatlidis, K., Moulin, M., Haertlein, M., and Timmins, P. (2008) Complementing structural information of modular proteins with small angle neutron scattering and contrast variation. *Eur. Biophys. J. 37* (5), 603–611.
38. Guan., J. Q., and Chance, M. R. (2005) Structural proteomics of macromolecular assemblies using oxidative footprinting and mass spectrometry. *Trends Biochem. Sci. 30*, 583–592.
39. Xu, G., and Chance, M. R. (2005) Radiolytic modification and reactivity of amino acid residues serving as structural probes for protein footprinting. *Anal. Chem. 77*, 4549–4555.
40. Takamoto, K., and Chance, M. R. (2006) Radiolytic protein footprinting with mass spectrometry to probe the structure of macromolecular complexes. *Annu. Rev. Biophys. Biomol. Struct. 35*, 251–276.
41. Gupta, S., Sullivan, M., Toomey, J., Kiselar, J., and Chance, M. R. (2007) The Beamline X28C of the Center for Synchrotron Biosciences: a national resource for biomolecular structure and dynamics experiments using synchrotron footprinting. *J. Synchrotron Radiat. 14*, 233–243.
42. Gupta, S., Cheng, H., Mollah, A. K., Jamison, E., Morris, S., Chance, M. R., Khrapunov, S., and Brenowitz, M. (2007) DNA and protein footprinting analysis of the modulation of DNA binding by the N-terminal domain of the *Saccharomyces cerevisiae* TATA binding protein. *Biochemistry 46*, 9886–9898.
43. Konarev, P. V., Petoukhov, M. V., Volkov, V. V., and Svergun, D. I. (2006) *ATSAS* 2.1, a program package for small-angle scattering data analysis. *J. Appl. Crystallogr. 39*, 277–286.
44. Lynn, G. W., Heller, W., Urban, V., Wignall, G. D., Weiss, K., and Myles, D. A. (2006) Bio-SANS: A dedicated facility for neutron structural biology at Oak Ridge National Laboratory. *Phys. B (Amsterdam, Neth.) 880*, 385–386.
45. Wignall, G. D., and Bates, F. S. (1987) Absolute Calibration Of Small-Angle Neutron-Scattering Data. *J. Appl. Crystallogr. 20*, 28–40.
46. Luo, G. M., Zhang, Q., Del Castillo, A. R., Urban, V., and O'Neill, H. (2009) Characterization of sol-gel-encapsulated proteins using small-angle neutron scattering. *ACS Appl. Mater. Interfaces 1* (10), 2262–2268.
47. Whitten, A. E., Cai, S., and Trewhella, J. (2008) *MULCh*: modules for the analysis of small-angle neutron contrast variation data from biomolecular assemblies. *J. Appl. Crystallogr. 41*, 222–226.
48. Zhang, Y. (2008) I-TASSER server for protein 3D structure prediction. *BMC Bioinformatics 9*, 40.
49. Jones, T. A., Zou, J. Y., Cowan, S. W., and Kjeldgaard, M. (1991) Improved methods for building protein models in electron density maps and the location of errors in these models. *Acta Crystallogr., Sect. A 47*, 110–119.
50. Kraulis, P. J. (1991) *MOLSCRIPT*: a program to produce both detailed and schematic plots of protein structures. *J. Appl. Crystallogr. 24*, 946–950.
51. Linding, R., Russell, R. B., Neduva, V., and Gibson, T. J. (2003) GlobPlot: exploring protein sequences for globularity and disorder. *Nucleic Acids Res. 31* (13), 3701–3708.
52. Ibel, K., and Stuhrmann, H. B. (1975) Comparison of neutron and X-ray scattering of dilute *myoglobin* solutions. *J. Mol. Biol. 93*, 255–265.
53. Volkov, V. V., and Svergun, D. I. (2003) Uniqueness of ab-initio shape determination in small-angle scattering. *J. Appl. Crystallogr. 36*, 860–864.
54. Petoukhov, M. V., Eady, N. A., Brown, K. A., and Svergun, D. I. (2002) Addition of missing loops and domains to protein models by x-ray solution scattering. *Biophys. J. 83* (6), 3113–3125.